

THE PARAMETRIC INSTABILITY OF ALFVÉN WAVES: EFFECTS OF TEMPERATURE ANISOTROPY

ANNA TENERANI, MARCO VELLI

Department of Earth, Planetary, and Space Sciences, University of California, Los Angeles, CA 90095

PETR HELLINGER

Astronomical Institute, CAS, Bocni II/1401, CZ-14100 Prague, Czech Republic

Draft version June 24, 2021

Abstract

We study the stability of large amplitude, circularly polarized Alfvén waves in an anisotropic plasma described by the double-adiabatic/CGL closure, and in particular the effect of a background thermal pressure anisotropy on the well-known properties of Alfvén wave parametric decay in Magnetohydrodynamics (MHD). Anisotropy allows instability over a much wider range of values of parallel plasma beta (β_{\parallel}) when $\xi = p_{0\perp}/p_{0\parallel} > 1$. When the pressure anisotropy exceeds a critical value, $\xi \geq \xi^*$ with $\xi^* \simeq 2.7$, there is a new regime in which the parametric instability is no longer quenched at high β_{\parallel} and in the limit $\beta_{\parallel} \gg 1$ the growth rate becomes independent of β_{\parallel} . In the opposite case of $\xi < \xi^*$, the instability is strongly suppressed with increasing parallel plasma beta, similarly to the MHD case. We analyze marginal stability conditions for parametric decay in the (ξ, β_{\parallel}) parameter space, and discuss possible implications for Alfvénic turbulence in the solar wind.

1. INTRODUCTION

Alfvén waves are ubiquitous in magnetized, astrophysical plasmas. They are invoked to explain the heating of stellar coronae and the acceleration of stellar winds, as well as the origin and formation of galactic and extragalactic jets (Jatenco-Pereira 1995). Since the first in-situ measurements (Unti & Neugebauer 1968), Alfvénic fluctuations have been commonly observed in the solar wind, especially in the fast streams possibly originating from coronal holes, from a few AU all the way down to 0.3 AU.

In the solar wind, Alfvénic fluctuations dominate the low frequency part of the fluctuation energy spectrum, with frequency f in the range $f \simeq 10^{-4} - 10^{-2}$ Hz. They appear to be mainly propagating outwards from the Sun and yet display a power-law spectrum that evolves with heliocentric distance (Bruno & Carbone 2013). One of the most remarkable properties observed during these so-called Alfvénic periods is that the amplitude of the magnetic field fluctuations $\delta\mathbf{B}$ is of the same order of the average, larger scale magnetic field \mathbf{B}_0 , i.e. they satisfy $|\delta\mathbf{B}|/|\mathbf{B}_0| \sim 1$. Despite such large excursions, the magnitude of the total magnetic field $|\mathbf{B}|$ remains relatively constant with negligible associated compressive fluctuations (Matteini et al. 2014, 2015). How is this Alfvénic turbulent state achieved in the solar wind, and what is its dynamical role in solar wind heating and acceleration remain fundamental open questions of Heliophysics and Astrophysics in general.

Large amplitude Alfvénic fluctuations with constant total (magnetic+kinetic) pressure constitute an exact nonlinear state in Magnetohydrodynamics (MHD). However, both theory (Galeev and Oraevskii 1973; Derby 1978) and numerical simulations (Del Zanna et al. 2001) show that such state is unstable and that Alfvénic fluctuations evolve by coupling with compressive and Alfvén

modes. This instability, called parametric instability or parametric decay, has proven to be robust and not significantly affected by wave polarization or propagation direction (Del Zanna 2001; Matteini et al. 2010). Even in the presence of a broad spectrum of frequencies, where one might expect a quenching due to the difficulty of maintaining resonance conditions, parametric decay has been shown to survive (Malara and Velli 1996; Malara et al. 2000). The parametric instability is more efficient at low values of the plasma beta (thermal to magnetic pressure ratio), $\beta \ll 1$. In this case, a forward propagating Alfvén wave with wave number k_0 , the mother wave, decays in two daughter waves: a forward sound wave with wave number $k_s \simeq 3/2k_0$ and a low frequency backward Alfvén wave with wave number $k_a = k_0 - k_s \simeq -k_0/2$. Such a decay tends to a four-wave interaction at larger β , including coupling with a forward Alfvén wave. However, parametric decay is strongly stabilized at values of β of order unity and beyond, unstable waves having amplitudes that scale as a positive power of β .

The solar wind expansion has been taken into account to investigate how it affects the parametric instability of waves launched from regions close to the Sun (Tenerani & Velli 2013). It was shown that the solar wind expansion stabilizes the frequencies with growth rate of the order or smaller than the expansion rate (frequencies of about 10^{-4} Hz), whereas the higher frequencies are unstable and decay during their propagation in the outer corona and inner heliosphere. In the solar wind, however, density fluctuations are extremely weak during Alfvénic periods, and the absence of signatures of Alfvén wave decay is mysterious. Dispersive effects due to finite ion inertial length or ion Larmor radius introduce a richer dynamics by breaking the symmetry between right and left hand polarizations and by allowing also modulational instabilities (Sakai & Sonnerup 1983; Wong & Goldstein 1986). The latter usually arise from the coupling of the mother wave with two forward daughter Alfvén waves,

one with frequency and wavenumber greater than that of the mother wave, and one with frequency and wavenumber smaller than that of the mother wave. In general, dispersion allows both modulational and parametric decay in regions where $\beta > 1$, extending the range of unstable modes (Hamabata 1993a; Vasquez 1995; Hollweg 1994; Araneda 1998; Nariyuki & Hada 2007; Araneda and Viñas 2008).

So far, research on the stability of large amplitude Alfvén waves and their nonlinear evolution has focused on (isotropic) plasmas in thermodynamic equilibrium. On the other hand, the weakly collisional solar wind displays several non-thermal features in the particle (proton) velocity distribution functions (PDF), especially in the fast streams (Marsch 2012). In particular, PDFs are often characterized by thermal anisotropies that vary with heliocentric distance most probably due to a combination of kinetic instabilities and expansion effects, which has not been described in detail. The PDFs are typically observed to be stable or marginally stable with respect to velocity-space instabilities driven by temperature anisotropies (Hellinger et al. 2006; Bale et al. 2009; Matteini et al. 2013).

Here we study the stability of large amplitude, circularly polarized Alfvén waves propagating in an anisotropic plasma by adopting the one fluid double adiabatic description of the plasma (Chew et al. 1956). We analyze how the background thermal anisotropy affects the properties of the parametric decay instability and we discuss under which conditions large amplitude Alfvén waves may be stable or not in the solar wind by providing diagrams in parameter space defined by the anisotropy vs. parallel plasma beta. Although we neglect dispersive, Landau damping and other kinetic effects, the present analysis is a first necessary step to understand the evolution of long wavelength Alfvén waves in the presence of velocity space anisotropies. We defer to later work the study of dispersion and kinetic effects. We note that a more limited study but in a similar vein was presented in Hamabata (1993b). However, because of some discrepancies in the relevant equations, we will not discuss that work here.

The remainder of the paper is organized as follows: in section 2 we define the initial configuration and address the general properties of the nonlinear wave equation resulting from the CGL model; in section 3 we study parametric decay of Alfvén waves in an anisotropic plasma and in section 4 we discuss possible implications for Alfvén waves in the solar wind; in section 5 we summarize our results.

2. MODEL EQUATIONS AND BACKGROUND CONFIGURATION

In this study we neglect dispersive effects due to finite Larmor radius (FLR) and ion inertial length by considering long wavelength and low frequency waves, so that the one fluid double adiabatic description of the plasma is suitable (Abraham-Shrauner 1967; Ferrière & André 2002; Cerri et al. 2013; Hunana et al. 2016; Del sarto et al. 2017). In general, different assumptions may be employed to close the hierarchy of equations obtained by taking the moments in velocity space of the Vlasov-Maxwell equations, each of them leading to different fluid models with approximated FLR and Landau

damping effects (Passot et al. 2012; Sulem & Passot 2015; Del sarto et al. 2016). For the purpose of this paper we adopt the well-known CGL framework in which not only dispersion, but also heat flux effects are entirely neglected (Chew et al. 1956). Despite these simplifying assumptions, the CGL model provides a good description of some effects due to thermal pressure anisotropy at the large scales, while a proper description of the dynamics at smaller scales would best require more sophisticated fluid models that include FLR effects (Hunana & Zank 2017) or even a full kinetic treatment. Ion-acoustic Landau damping may be modeled phenomenologically by adding an appropriate drag term to the longitudinal component of the momentum equation. This approach was employed to study how Landau damping affects parametric and modulational instabilities in fluid models, and it was shown to lead to results consistent with the outcome of hybrid simulations (Vasquez 1995; Gomberoff 2000). In particular, Landau damping reduces the growth rate of parametric decay at most by a factor of order two. For this reason, we have decided not to include it here, although it may be of interest to inspect its effects in future works devoted to more general, non-monochromatic waves (Cohen & Dewar 1974).

The CGL model is given by the following set of equations,

$$\frac{\partial \rho}{\partial t} + \nabla \cdot (\rho \mathbf{u}) = 0 \quad (1)$$

$$\rho \left(\frac{\partial \mathbf{u}}{\partial t} + \mathbf{u} \cdot \nabla \mathbf{u} \right) = -\nabla \left(p_{\perp} + \frac{B^2}{8\pi} \right) + \frac{1}{4\pi} \mathbf{B} \cdot \nabla \mathbf{B} + \nabla \cdot (\hat{\mathbf{b}} \hat{\mathbf{b}} \Delta p), \quad (2)$$

$$\frac{\partial \mathbf{B}}{\partial t} = \nabla \times (\mathbf{u} \times \mathbf{B}), \quad (3)$$

$$\left(\frac{\partial}{\partial t} + \mathbf{u} \cdot \nabla \right) \left(\frac{p_{\parallel} B^2}{\rho^3} \right) = 0, \quad (4)$$

$$\left(\frac{\partial}{\partial t} + \mathbf{u} \cdot \nabla \right) \left(\frac{p_{\perp}}{\rho B} \right) = 0, \quad (5)$$

where $\hat{\mathbf{b}} = \mathbf{B}/B$ is the unit vector along the magnetic field, $B = |\mathbf{B}|$ is the magnetic field magnitude and $\Delta p = p_{\perp} - p_{\parallel}$, perpendicular and parallel referring to the magnetic field \mathbf{B} .

Just as in MHD, perfectly correlated finite amplitude transverse magnetic and velocity fluctuations are an exact nonlinear state, or dynamical equilibrium, of Eqs. (1)–(5), provided the total (kinetic+magnetic) pressure is homogeneous (constant in space). The (one-dimensional) wave equation resulting from the CGL model, Eq. (17) below, however contains a nonlinear term which is absent in MHD, in that the fluctuation propagation speed depends on the magnetic pressure of the fluctuation itself. This nonlinearity has important effects: it regularizes firehose unstable fluctuations that would grow without bounds in the linear approximation, and allows a class of nonlinear states that cannot be reduced to a simple superposition of monochromatic waves. Depending upon the initial conditions, this class

of solutions includes as particular case circularly polarized Alfvén waves (i.e. temporally constant amplitude waves).

Although many initial conditions can in principle be considered to study parametric decay, in this work we focus on the stability of circularly polarized Alfvén waves. We review this specific case below, followed by a discussion on the evolution of fluctuations in the firehose unstable regime and on the properties of the nonlinear wave equation.

2.1. Nonlinear circularly polarized Alfvén waves in anisotropic plasmas

We begin by seeking for solutions to the CGL equations that correspond to circularly polarized plane waves propagating along the z direction. Those exact solutions will define the dynamical equilibrium for the subsequent linear stability analysis described in section 3.

To this end, consider a uniform magnetized plasma with density ρ_0 , magnetic field $\mathbf{B}_0 = B_0 \hat{\mathbf{z}}$ (say, $B_0 > 0$) and parallel and perpendicular pressures $p_{0\parallel}$ and $p_{0\perp}$, respectively. Also, since we are interested in plane waves, the longitudinal velocity and magnetic field U_z and B_z are set to zero. Transverse velocity and magnetic field fluctuations, labelled respectively $\mathbf{U}_\perp(z, t)$ and $\mathbf{B}_\perp(z, t)$, with constant and homogeneous magnetic pressure (i.e. $|\mathbf{B}_\perp| = \text{const.}$) obey to the following coupled differential equations:

$$\frac{\partial \mathbf{U}_\perp}{\partial t} = \frac{B_0}{4\pi\rho_0} \frac{\partial}{\partial z} \mathbf{B}_\perp + \frac{1}{\rho_0} \frac{\partial}{\partial z} \left(\frac{B_0 \mathbf{B}_\perp}{B_\perp^2 + B_0^2} \Delta p_0 \right), \quad (6)$$

$$\frac{\partial \mathbf{B}_\perp}{\partial t} = B_0 \frac{\partial}{\partial z} \mathbf{U}_\perp. \quad (7)$$

Note that the above equations remain valid also in cases where the total magnetic pressure is not uniform. In the latter case however, the full complement of the double adiabatic and continuity equations would need to be considered to solve Eqs. (6)–(7). Here we will always be concerned with the special case in which the total magnetic pressure is uniform in space.

After introducing the normalized magnetic field $\hat{\mathbf{B}}_\perp = \mathbf{B}_\perp/B_0$ and the Alfvén speed $V_a = B_0/\sqrt{4\pi\rho_0}$, we can combine eqs. (6)–(7) so as to obtain the following wave equation:

$$\frac{\partial^2}{\partial t^2} \hat{\mathbf{B}}_\perp(z, t) = \left(V_a^2 + \frac{1}{\rho_0} \frac{\Delta p_0}{1 + \hat{B}_\perp^2} \right) \frac{\partial^2}{\partial z^2} \hat{\mathbf{B}}_\perp(z, t). \quad (8)$$

Provided the condition

$$\tilde{V}_a^2 = V_a^2 + \frac{1}{\rho_0} \frac{\Delta p_0}{1 + \hat{B}_\perp^2} > 0 \quad (9)$$

is satisfied, Eq. (8) describes Alfvén waves, either left or right handed polarized, that propagate at the speed \tilde{V}_a . Forward (upper sign) and backward (lower sign) propagating waves have the following general form:

$$\hat{\mathbf{B}}_\perp(z, t) = \hat{B}_\perp \Re \left[e^{if(z \mp \tilde{V}_a t)} (\hat{\mathbf{x}} - i\hat{\mathbf{y}}) \right], \quad (10)$$

$$\mathbf{U}_\perp(z, t) = \mp \tilde{V}_a \hat{\mathbf{B}}_\perp(z, t), \quad (11)$$

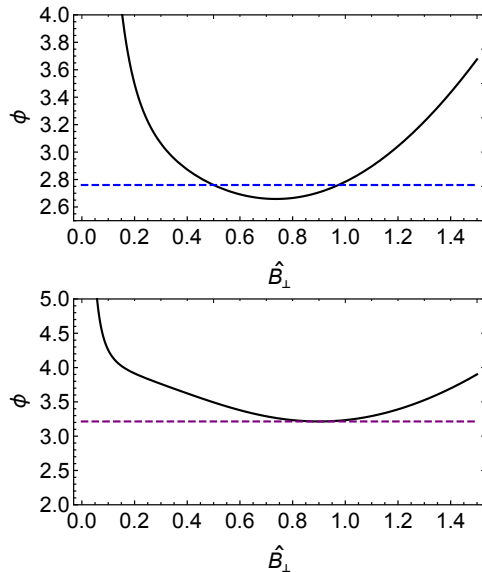


Figure 1. Plot of the potential ϕ (solid black lines) and of the total energy E (dashed lines) vs. the amplitude \hat{B}_\perp for $\beta_\parallel = 4$ and anisotropic pressure ratio $\xi = 0.1$: the upper panel corresponds to a fluctuation in the firehose regime with $\hat{B}_\perp(0) = 0.5$; the lower panel corresponds to a circularly polarized Alfvén wave with $\hat{B}_\perp(0) = 0.9$.

where for the sake of illustration a left-hand polarization has been chosen.

2.2. General properties of the CGL nonlinear wave equation and “firehose” fluctuations

The condition $\tilde{V}_a^2 = 0$, with \tilde{V}_a^2 given by Eq. (9), generalizes the well-known threshold separating Alfvén waves from exponentially growing firehose fluctuations by including the nonlinear effect of the fluctuation magnetic pressure – for a discussion on the firehose instability in the small amplitude limit see e.g. Hunana & Zank (2017). By analogy with the traditional firehose stability condition, the inequality $\tilde{V}_a^2 > 0$ may be expressed in terms of the total magnetic pressure or, in non dimensional form, in terms of the total parallel plasma beta β_\parallel^\top and ξ , defined respectively by

$$\beta_\parallel^\top = 8\pi \frac{p_{0\parallel}}{B_0^2} \frac{1}{1 + \hat{B}_\perp^2} \quad \text{and} \quad \xi = \frac{p_{0\perp}}{p_{0\parallel}}, \quad (12)$$

$$(\xi - 1) \frac{\beta_\parallel^\top}{2} > -1. \quad (13)$$

It is however convenient to leave the amplitude \hat{B}_\perp as a free parameter and to define β_\parallel by means of the background magnetic field, i.e.

$$\beta_\parallel = p_{0\parallel} \frac{8\pi}{B_0^2}. \quad (14)$$

For small amplitude fluctuations the firehose instability is obtained when

$$(\xi - 1) \frac{\beta_\parallel}{2} < -1; \quad (15)$$

however, inclusion of finite amplitude effects leads to a critical amplitude \hat{B}^* above which the condition $\tilde{V}_a^2 > 0$

remains satisfied, and therefore waves may still propagate if of sufficiently large amplitude:

$$\hat{B}_\perp > \hat{B}_\perp^* = \left[\frac{1}{2} \beta_\parallel (1 - \xi) - 1 \right]^{1/2}. \quad (16)$$

Consider now the case of a firehose unstable fluctuation, with a very small initial amplitude $\hat{B}_\perp(0) \ll \hat{B}_\perp^*$. Clearly, the amplitude starts to grow exponentially as predicted by the linear theory, approaching the value of \hat{B}_\perp^* . At that point finite amplitude effects come into play in a non trivial way preventing the fluctuation from growing without bounds. In order to understand the temporal evolution of fluctuations in this regime ($\tilde{V}_a^2 < 0$) we briefly discuss below the behavior of nonlinear solutions with time-dependent amplitude.

Nonlinear solutions that generalize circularly polarized Alfvén waves must satisfy the following nonlinear wave equation:

$$\frac{\partial^2}{\partial t^2} \hat{\mathbf{B}}_\perp(z, t) = \left(V_a^2 + \frac{1}{\rho_0} \frac{\Delta p(t)}{1 + \hat{B}_\perp^2(t)} \right) \frac{\partial^2}{\partial z^2} \hat{\mathbf{B}}_\perp(z, t), \quad (17)$$

where Δp evolves in time according to Eqs. (4)–(5). The latter can be integrated to obtain the following expression:

$$\Delta p(t) = \left[p_{0\perp} \sqrt{\frac{1 + \hat{B}_\perp^2(t)}{1 + \hat{B}_\perp^2(0)}} - p_{0\parallel} \frac{1 + \hat{B}_\perp^2(0)}{1 + \hat{B}_\perp^2(t)} \right]. \quad (18)$$

The boundedness of solutions of Eq. (17) can be demonstrated from first principles for a single Fourier mode with wave vector k_0 by deriving the corresponding energy conservation equation. In this case fluctuations with homogeneous magnetic pressure can be written in the following form,

$$\begin{aligned} \hat{B}_x(z, t) &= \Re[B_{k_0}(t)e^{ik_0z}], \\ \hat{B}_y(z, t) &= \Im[B_{k_0}(t)e^{ik_0z}], \end{aligned} \quad (19)$$

where B_{k_0} is the complex time dependent amplitude. A standard manipulation of Eq. (17) leads to the total energy (E) conservation equation, involving the square amplitude of the fluctuation ($\hat{B}_\perp^2 = \hat{B}_x^2 + \hat{B}_y^2$), its square temporal derivative (denoted with a dot, $\dot{\hat{B}}_\perp^2 = (\dot{\hat{B}}_x)^2 + (\dot{\hat{B}}_y)^2$) and the effective potential (ϕ):

$$\dot{\hat{B}}_\perp^2 + \phi = E. \quad (20)$$

By defining $\omega_A^2 = k_0^2 V_a^2$ and $L = 2\hat{B}_\perp^2 \dot{\theta}$, where L is a constant determined by the initial conditions, θ being the angle between \hat{B}_y and \hat{B}_x , the potential ϕ can be written in compact form as

$$\begin{aligned} \phi &= \omega_A^2 \hat{B}_\perp^2 + \frac{1}{4} \frac{L^2}{\hat{B}_\perp^2} + \\ &\omega_A^2 \frac{\beta_\parallel}{2} \left(2\xi \frac{\sqrt{1 + \hat{B}_\perp^2}}{\sqrt{1 + \hat{B}_\perp^2(0)}} + \frac{1 + \hat{B}_\perp^2(0)}{1 + \hat{B}_\perp^2} \right). \end{aligned} \quad (21)$$

Equations (20)–(21) show that the system is equivalent to the motion of a particle subject to a central field of

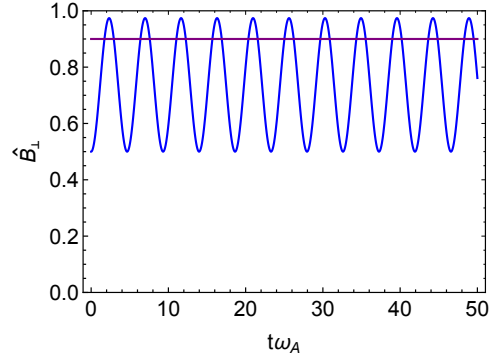


Figure 2. Temporal evolution of the amplitude of a circularly polarized Alfvén wave (purple color) and of a non-constant amplitude fluctuation in the firehose regime (blue color), for the same parameters given in Fig. 1.

force, where the perpendicular amplitude and its temporal derivative play the role of the particle position and velocity, respectively, L is the particle angular momentum and ϕ is the potential energy which is a function of coordinates. The first term on the right hand side of Eq. (21) corresponds to the harmonic potential, the second term is the counterpart of the centrifugal potential and the last term is introduced by the double adiabatic closure. At large amplitudes the harmonic potential dominates, and therefore ϕ behaves as a potential well for any β_\parallel and ξ . As a consequence, there are no unbounded solutions for firehose unstable fluctuations: minima and maxima of the wave amplitude are the turning points corresponding to $E = \phi$, whereas constant amplitude waves (i.e. circularly polarized waves) lie in the potential minimum.

As an example, we show in Fig. 1 the plot of ϕ for $\xi = 0.1$ and $\beta_\parallel = 4$, therefore for the more interesting case that can be in the firehose regime depending upon the initial amplitude. Dashed lines correspond to the total energy E fixed by the initial conditions, that we show for two cases: for $\hat{B}_\perp(0) = 0.5$, smaller than \hat{B}_\perp^* (upper panel), and for $\hat{B}_\perp(0) = 0.9$, larger than \hat{B}_\perp^* (lower panel). In Fig. 2 and 3 we plot the magnitude of $\hat{B}_\perp(t)$ as a function of time and its polarization at a fixed point in space, respectively, for the same two cases indicated in Fig. 1. The plotted solutions were obtained by integrating numerically Eq. (17) for a monochromatic wave and by imposing initial conditions that correspond to a forward circularly polarized wave: $\hat{B}_x(0) = \hat{B}_\perp(0)$, $\hat{B}_y(0) = 0$ and $\dot{\hat{B}}_x(0) = 0$, $\dot{\hat{B}}_y(0) = -\omega_A(|\tilde{V}_a(0)|/V_a)\hat{B}_\perp(0)$. As expected, for $\hat{B}_\perp(0) > \hat{B}_\perp^*$ (purple color in Fig. 2 and 3) the amplitude of the wave remains constant and has minimum potential energy (see Fig. 1, lower panel), corresponding to a circularly polarized wave; in the case $\hat{B}_\perp(0) < \hat{B}_\perp^*$ (blue color in Fig. 2 and 3), the fluctuation is initially in the firehose regime and its amplitude oscillates between the two turning points $\hat{B}_\perp = 0.5$ and $\hat{B}_\perp = 0.98$ (see Fig. 1, upper panel).

In conclusion, in the framework of the CGL model the firehose threshold does not represent a stability condition for fluctuations with spatially homogeneous (total) pressure, but rather it represents a condition for the existence of time-constant amplitude waves. Below that threshold the wave amplitude has to be an evolving function of time, so that the condition $|\mathbf{B}_\perp| = \text{const}$ cannot be sat-

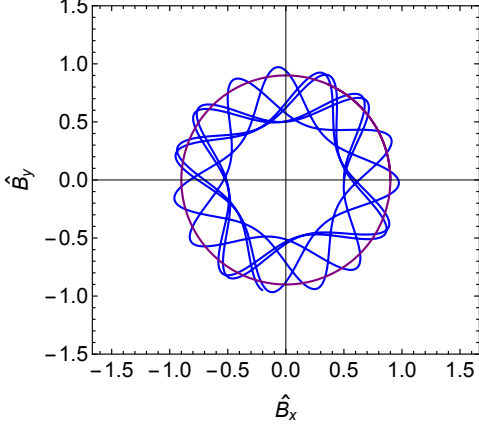


Figure 3. Polarization parameterized in time for the circularly polarized wave and the fluctuation in the firehose regime described in Fig. 1–2.

ified. Eq. (16) therefore provides a lower limit for the amplitude of Alfvén waves below which circularly polarized Alfvén waves cannot exist, that at large β_{\parallel} roughly scales as

$$\hat{B}_{\perp}^* \sim \beta_{\parallel}^{1/2}. \quad (22)$$

It is worthwhile to notice that the scaling given in Eq. (22) has an opposite trend with β_{\parallel} with respect to the one found by Squire et al. (2016), who studied finite amplitude effects on the propagation of linearly polarized Alfvén waves at very large β_{\parallel} . They found an amplitude upper limit \hat{B}_{\perp}^{max} scaling as $\hat{B}_{\perp}^{max} \sim \beta^{-1/2}$ (β defined with an average pressure $p_0 = 2/3 p_{0\perp} + 1/3 p_{0\parallel}$), above which Alfvén waves become strongly modified by a self-induced firehose instability: the temporal and spatial modulations of the total magnetic field magnitude lead to variations of Δp that drives the system towards the firehose unstable threshold thereby “interrupting” the wave. The latter evolves into a sequence of spatial discontinuities so as to minimize \hat{B}_{\perp}^2 due to a third order effect in the wave amplitude. This mechanism does not take place in our case, where we consider fluctuations with a constant magnitude of the magnetic field. However, we conjecture that at large β_{\parallel} any perturbation above a circularly polarized state will return the field to a configuration of total constant magnetic field magnitude rather than the “interrupted” profiles seen starting from linear polarization. Indeed we believe this process may be at work in the formation of the constant amplitude Alfvén waves seen in the solar wind, a question that will be explored in a subsequent paper. Such a mechanism cannot be captured in the present study where we retain up to first order terms in the perturbation amplitude.

3. PARAMETRIC INSTABILITY: RESULTS

We now take a monochromatic, left-hand circularly polarized mother Alfvén wave in parallel propagation with magnetic and velocity field as given below,

$$\hat{\mathbf{B}}_{\perp} = \hat{B}_{\perp} e^{i(k_0 z - \omega_0 t)} (\hat{\mathbf{x}} - i\hat{\mathbf{y}}), \quad (23)$$

$$\mathbf{U}_{\perp} = -\tilde{V}_a \hat{\mathbf{B}}_{\perp}, \quad (24)$$

$$\omega_0 = \tilde{V}_a k_0, \quad (25)$$

and, following the standard method, we study its stability with respect to small perturbations in velocity, pressure, density and magnetic field. Perturbations are of the form

$$u_{\parallel} e^{i(kz - \omega t)}, \quad u_{\pm} e^{i(k \pm k_0)z - i(\omega \pm \omega_0)t}, \quad (26)$$

$$p_{\parallel(\perp)} e^{i(kz - \omega t)}, \quad \rho e^{i(kz - \omega t)}, \quad (27)$$

$$\hat{b}_{\pm} e^{i(k \pm k_0)z - i(\omega \pm \omega_0)t}, \quad (28)$$

where $u_{\pm} = u_y \pm iu_z$ and similarly $\hat{b}_{\pm} = \hat{b}_y \pm i\hat{b}_z$. Linearization of the parent system of Eqs. (1)–(5) around the configuration given in Eqs. (23)–(24), leads to the following set of algebraic equations,

$$\omega \frac{\rho}{\rho_0} - k u_{\parallel} = 0 \quad (29)$$

$$(\omega \pm \omega_0) \hat{b}_{\pm} + (u_{\pm} - \hat{B}_{\perp} u_{\parallel})(k \pm k_0) = 0 \quad (30)$$

$$\omega u_{\parallel} = k \frac{p_{\perp}}{\rho_0} + \hat{B}_{\perp} k (\hat{b}_{+} + \hat{b}_{-}) \left(\frac{1}{2} V_a^2 + \frac{\Delta p_0}{\rho_0 (1 + \hat{B}_{\perp}^2)} \right) - k \frac{\Delta p}{\rho_0 (1 + \hat{B}_{\perp}^2)} \quad (31)$$

$$\begin{aligned} (\omega \pm \omega_0) u_{\pm} \pm \frac{\rho}{\rho_0} \omega_0 u_{0\pm} \mp k_0 u_{0\pm} u_{\parallel} = & -V_a^2 (k \pm k_0) \hat{b}_{\pm} \\ & - (k \pm k_0) \left[\frac{\Delta p_0}{\rho_0 (1 + \hat{B}_{\perp}^2)} \hat{b}_{\pm} + \frac{\hat{B}_{\perp}}{1 + \hat{B}_{\perp}^2} \frac{\Delta p}{\rho_0} \right. \\ & \left. - \frac{\hat{B}_{\perp}^2}{(1 + \hat{B}_{\perp}^2)^2} \frac{\Delta p_0}{\rho_0} (\hat{b}_{+} + \hat{b}_{-}) \right] \end{aligned} \quad (32)$$

$$p_{\parallel} = p_{0\parallel} \left[3 \frac{\rho}{\rho_0} - \frac{\hat{B}_{\perp}}{1 + \hat{B}_{\perp}^2} (\hat{b}_{+} + \hat{b}_{-}) \right] \quad (33)$$

$$p_{\perp} = p_{0\perp} \left[\frac{\rho}{\rho_0} + \frac{1}{2} \frac{\hat{B}_{\perp}}{1 + \hat{B}_{\perp}^2} (\hat{b}_{+} + \hat{b}_{-}) \right] \quad (34)$$

$$\begin{aligned} \Delta p = & \frac{\rho}{\rho_0} (p_{0\perp} - 3p_{0\parallel}) + \\ & \frac{\hat{B}_{\perp}}{1 + \hat{B}_{\perp}^2} (\hat{b}_{+} + \hat{b}_{-}) \left(\frac{1}{2} p_{0\perp} + p_{0\parallel} \right). \end{aligned} \quad (35)$$

The dispersion relation for the complex frequencies relative to Eqs. (29)–(35) can be written in implicit form as follows:

$$\left[\hat{\omega}^2 - \tilde{\beta} \hat{k}^2 \left(1 + \frac{\hat{B}_\perp^2 \xi}{3} \right) \right] \left\{ (\hat{\omega} - \hat{k}) [(\hat{\omega} + \hat{k})^2 - 4] + \frac{\tilde{\beta} \hat{B}_\perp^2 (\xi - 4)}{3(1 + \hat{B}_\perp^2)} [(\hat{k}^2 + 1)\hat{\omega} + \hat{k}(\hat{k}^2 - 3)] \right\} \\ = \hat{B}_\perp^2 \hat{k}^2 \left[1 - \frac{\tilde{\beta}(3 - \xi - \hat{B}_\perp^2)}{3(1 + \hat{B}_\perp^2)} \right] \left\{ (\hat{\omega}^3 + \hat{\omega}^2 \hat{k} - 3\hat{\omega} + \hat{k}) - \frac{\tilde{\beta}(3 - \xi)}{3} [(\hat{k}^2 + 1)\hat{\omega} + \hat{k}(\hat{k}^2 - 3)] \right\}. \quad (36)$$

Equation (36) is expressed in normalized units with speeds normalized to \tilde{V}_a and frequencies to ω_0 . For the sake of notation we have defined

$$\hat{\omega} = \omega/\omega_0, \quad \hat{k} = k/k_0, \quad (37)$$

and the parameter $\tilde{\beta}$ is defined as

$$\tilde{\beta} = \frac{3}{2} \frac{\beta_\parallel}{1 + \hat{B}_\perp^2 + \frac{\beta_\parallel}{2}(\xi - 1)}. \quad (38)$$

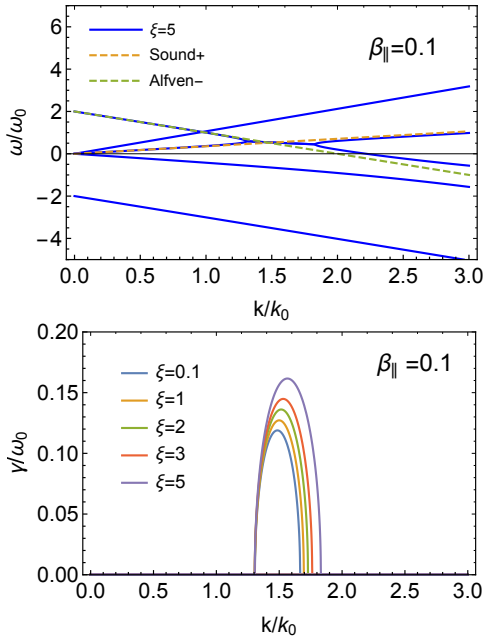


Figure 4. Normalized frequency ω/ω_0 and growth rate γ/ω_0 vs. k/k_0 for $\beta_\parallel = 0.1$ and $\hat{B}_\perp^2 = 0.1$ at different anisotropic pressure ratio ξ .

The dispersion relation given in Eq. (36) is a fifth order equation in $\hat{\omega}$ that we have solved numerically for different values of the plasma parameters \hat{B}_\perp^2 , ξ and β_\parallel . We therefore prefer to use the plasma beta β_\parallel defined with the magnitude of the average magnetic field B_0 (see Eq. 14) instead of β_\parallel^2 or $\tilde{\beta}$, so that all plasma parameters are independent from each other.

In Fig. 4 and 5 we show the real part of the dispersion relation ($\omega(k)$, upper panel) for anisotropic pressure ratio $\xi = 5$ and the imaginary part ($\gamma(k)$, lower panel) for different values of ξ at fixed $\hat{B}_\perp^2 = 0.1$ and, respectively, $\beta_\parallel = 0.1$ and $\beta_\parallel = 1$. For clarity, we also display in dashed lines the dispersion relation of the two main interacting branches for $\hat{B}_\perp^2 = 0$: the sound branch $\omega = \tilde{V}_a \hat{\beta}^{1/2} k$ in orange and the backward Alfvén branch

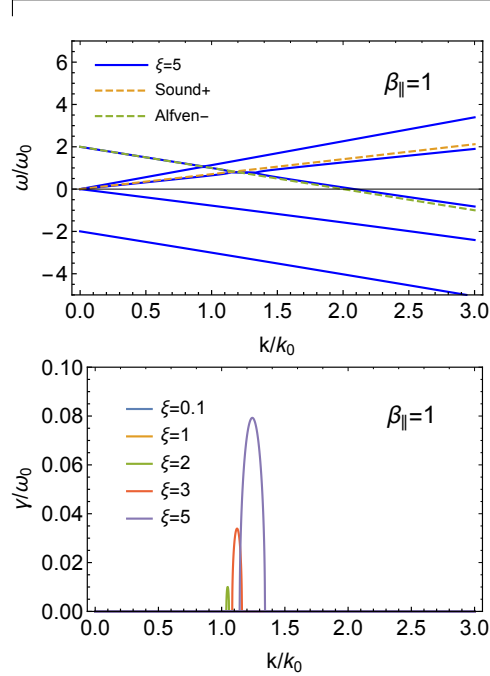


Figure 5. Normalized frequency ω/ω_0 and growth rate γ/ω_0 vs. k/k_0 for $\beta_\parallel = 1$ and $\hat{B}_\perp^2 = 0.1$ at different anisotropic pressure ratio ξ .

$\omega = -\tilde{V}_a(k - k_0) + \omega_0$ in green. As can be seen by inspection, there is a range of wave vectors unstable to the parametric decay due to the coupling between a forward sound wave with $k > k_0$ and a low frequency backward right-handed Alfvén wave, with wave vector $k_- = k - k_0$ and frequency $\omega_- = \omega - \omega_0$. At larger β_\parallel the interaction becomes a four-wave interaction including also a forward Alfvén wave. Fig. 4 and 5 (bottom panels) show that in general the range of unstable modes and the growth rate increase with ξ and that, provided ξ is large enough, parametric decay can occur for relatively small amplitudes (e.g. $\hat{B}_\perp^2 = 0.1$) even at large plasma beta (e.g. $\beta_\parallel \simeq 1$), contrary to the MHD model.

The background pressure anisotropy affects the properties of the instability in different ways depending upon the value of β_\parallel . In the limit $\beta_\parallel \rightarrow 0$ the dispersion relation given in Eq. (36) is independent from both β_\parallel and ξ , and the known MHD results are therefore recovered for small values of β_\parallel ¹. Interestingly, growth rates are independent from β_\parallel also in the opposite limit $\beta_\parallel \rightarrow \infty$, but in this case growth rates still depend on ξ ². Numerical inspection of Eq. (36) within this limit (where only the case $\xi \geq 1$ is considered for consistency with the firehose

¹ The limit $\beta_\parallel \rightarrow 0$ of Eq. (36) is: $\hat{\omega}^2(\hat{\omega} - \hat{k})[(\hat{\omega} + \hat{k})^2 - 4] = \hat{B}_\perp^2 \hat{k}^2(\hat{\omega}^3 + \hat{\omega}^2 \hat{k} - 3\hat{\omega} + \hat{k})$. This corresponds to the MHD dispersion relation of the parametric decay in a cold plasma (Derby 1978).

² A way to see this is by considering that if $\beta \rightarrow \infty$ then $\tilde{\beta} \rightarrow 3/(\xi - 1)$.

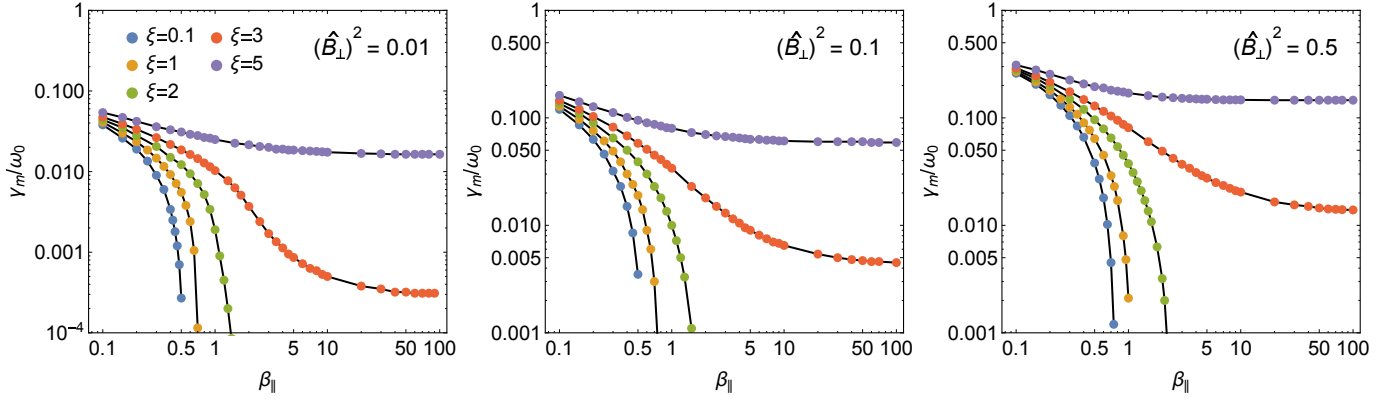


Figure 6. Maximum growth rates γ_m/ω_0 as a function of β_{\parallel} at different anisotropic pressure ratio ξ , for $\hat{B}_{\perp}^2 = 0.01$ (left panel), $\hat{B}_{\perp}^2 = 0.1$ (middle panel) and $\hat{B}_{\perp}^2 = 0.5$ (right panel).

threshold) shows that, at given amplitude, growth rates are greater than zero if the anisotropic pressure ratio is above a critical value $\xi^* \simeq 2.67$. This implies that the parametric decay instability has growth rates $\gamma(k)$ that decrease and tend to zero as β_{\parallel} increases (unless the amplitude of the mother wave increases with β_{\parallel}) if $\xi < \xi^*$, while it reaches finite and constant $\gamma(k)$ for $\beta_{\parallel} \gg 1$ if $\xi \geq \xi^*$.

The existence of these two regimes at large β_{\parallel} is confirmed by Fig. 6, where we show the normalized maximum growth rate γ_m/ω_0 as a function of β_{\parallel} for different values of ξ and \hat{B}_{\perp}^2 . As can be seen by inspection of the displayed plots, if $\xi < \xi^*$ the maximum growth rate decreases as β_{\parallel} increases, similarly to what happens in the MHD model. On the contrary, for $\xi > \xi^*$ the maximum growth rate becomes weakly dependent on β_{\parallel} as the latter increases, and it tends to a constant value for $\beta_{\parallel} \gg 1$. At given amplitude, all curves γ_m converge towards the same value for $\beta_{\parallel} \ll 1$.

Another useful way to display our results is to plot the contours of the maximum growth rates in parameter space. In Fig. 7 and 8 we show the contours corresponding to $\gamma_m/\omega_0 = 0.01, 0.05, 0.1$ (blue lines) together with the contour line corresponding to $\tilde{V}_a^2 = 0$ (red line). The region above of the red line is unstable to parametric decay, while the region below the red line has not been considered in this study.

In Fig. 7 we display the contours in the (ξ, β_{\parallel}) plane for three fixed square amplitudes of the mother wave, $\hat{B}_{\perp}^2 = 0.5$ (left panel), $\hat{B}_{\perp}^2 = 0.5$ and $\hat{B}_{\perp}^2 = 1$ (right panel). As can be seen, growth rates do not depend on the plasma beta at large β_{\parallel} , whereas for small β_{\parallel} they essentially are unaffected by the anisotropy. As the amplitude increases, contours display the same trends but they are shifted towards larger β_{\parallel} and smaller ξ values. The firehose threshold is also shifted, in this case due to the fact that larger amplitudes have a higher threshold (cfr. Eq. 16). In Fig. 8 the same growth rates are shown in the $(\hat{B}_{\perp}, \beta_{\parallel})$ plane for $\xi = 5$, larger than ξ^* (left panel), $\xi = 1$ (middle panel) and $\xi = 0.1$, smaller than ξ^* (right panel). These plots also clearly show the existence of two regimes: if $\xi > \xi^*$ then the growth rates become independent on β_{\parallel} and hence the amplitudes saturate at $\beta_{\parallel} \gg 1$ (Fig. 8 left panel); if instead $\xi < \xi^*$, then the trends are similar to those found in MHD, with

the parametric instability being strongly stabilized as β_{\parallel} increases. In this regime of anisotropy amplitudes can be extremely large. In particular, amplitudes scale as $\hat{B}_{\perp} \sim \beta_{\parallel}^{1/2}$, for $\beta_{\parallel} \gg 1$ and fixed γ_m , like the firehose threshold (Fig. 8, middle and right panels).

4. DISCUSSION: THE PARAMETRIC INSTABILITY IN THE SOLAR WIND

In this section we compare our results with solar wind data. Previous numerical work using the MHD (accelerating) expanding box has shown that the solar wind expansion stabilizes parametric decay unless the growth rate is larger than the expansion rate $\tau_e^{-1} \simeq U_{sw}/r$, where U_{sw} is the solar wind speed and r is the heliocentric distance. The condition $\gamma_m \tau_e \simeq 1$ can therefore be used now as a criterion for the onset of parametric decay in the solar wind. By fixing $U_{sw} = 700$ km/s, we estimate that for low frequencies $\omega_0^L \simeq 2\pi \times 10^{-4}$ Rad/s and high frequencies $\omega_0^H \simeq 2\pi \times 10^{-2}$ Rad/s, the normalized expansion rates are respectively $1/(\tau_e \omega_0^L) \simeq 10^{-2}$ and $1/(\tau_e \omega_0^H) \simeq 10^{-4}$, at $r = 0.9$ AU, and $1/(\tau_e \omega_0^L) \simeq 2 \times 10^{-2}$ and $1/(\tau_e \omega_0^H) \simeq 2 \times 10^{-4}$ at $r = 0.3$ AU.

Fig. 9 displays diagrams in the parameter space (β_{\parallel}, ξ) of the stable and unstable regions to parametric decay at $r = 0.9$ AU (upper panel) and $r = 0.3$ AU (lower panel): blue lines correspond to the contour $\gamma_m \tau_e = 1$ for ω_0^L (solid line) and for ω_0^H (dashed line), whereas the red dot indicates the location in the diagram of the average fast solar wind. In order to plot the contours, we estimated the normalized square amplitudes $(\hat{B}_{\perp}^{L,H})^2$ that correspond to $\omega_0^{L,H}$ from the spectra measured by the Helios spacecraft in the Alfvénic wind (see e.g. Bruno & Carbone (2013)): $(\hat{B}_{\perp}^L)^2 \simeq 0.1$ and $(\hat{B}_{\perp}^H)^2 \simeq 0.01$ at $r = 0.9$ AU, and $(\hat{B}_{\perp}^L)^2 \simeq 0.06$ and $(\hat{B}_{\perp}^H)^2 \simeq 0.05$ at $r = 0.3$ AU. To estimate the average values of $\beta_{\parallel}(r)$, $\xi(r)$ and $B_0(r)$ we used the fast wind empirical profiles discussed in Hellinger et al. (2011). Since the low frequency fluctuations are stabilized by the expansion more than the high frequency ones, their threshold provides an upper limit for the stability of a broader spectrum of fluctuations, above which all frequencies are expected to be unstable (white region: $\gamma \tau_e > 1$ for $\omega_0 > \omega_0^L$). Viceversa, below the threshold for the highest frequencies the whole spectrum is stable (light blue region: $\gamma \tau_e < 1$ for $\omega_0 < \omega_0^H$). In the yellow region instead the intermediate

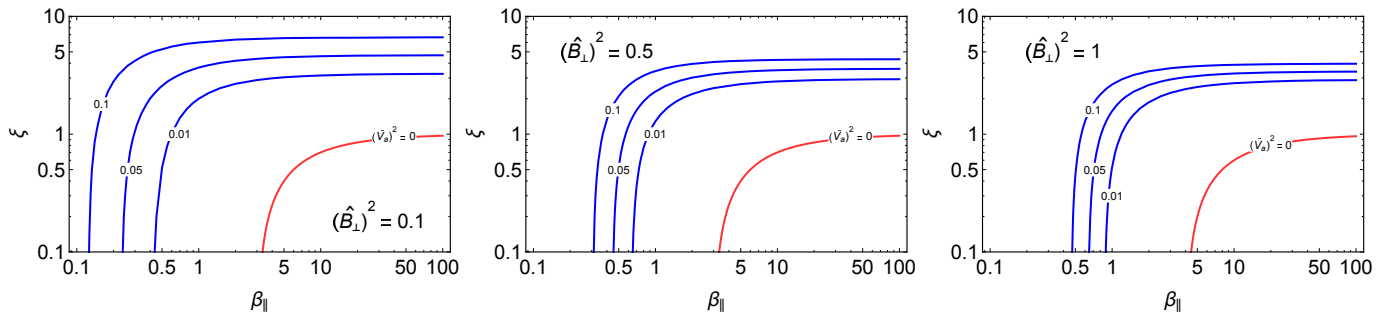


Figure 7. Contours of the normalized maximum growth rate $\gamma_m/\omega_0 = 0.01, 0.05, 0.1$ in the parameter space (ξ, β_{\parallel}) (blue lines) and the threshold given by Eq. (16) (red line), for $\hat{B}_{\perp}^2 = 0.1$ (left panel), $\hat{B}_{\perp}^2 = 0.5$ (middle panel) and $\hat{B}_{\perp}^2 = 1$ (right panel).

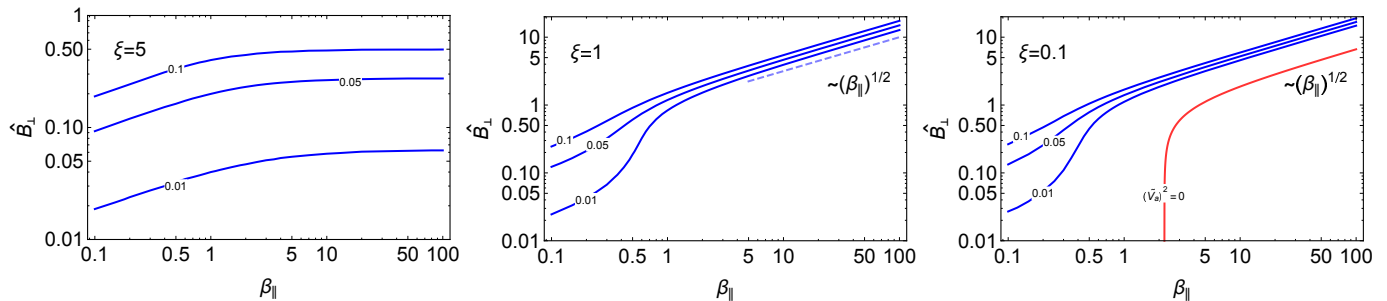


Figure 8. Contours of the normalized maximum growth rate $\gamma_m/\omega_0 = 0.01, 0.05, 0.1$ in the parameter space $(\hat{B}_{\perp}, \beta_{\parallel})$ (blue lines) for $\xi = 5$ (left panel), $\xi = 1$ (middle panel) and $\xi = 0.1$ (right panel). The red line corresponds to the threshold given in Eq. (16). At large β_{\parallel} the amplitude of a parametrically unstable Alfvén wave scales as $\sim \beta_{\parallel}^{1/2}$, at given γ_m .

frequencies $\omega_0^L < \omega_0 < \omega_0^H$ are unstable.

The diagrams displayed in Fig. 9 show that the average fast solar wind is close to the stable region at $r = 0.9$ AU, while at $r = 0.3$ AU it moves towards the unstable one. Of course, these diagrams should be regarded as indicative, since slightly different estimations for the expansion rates and amplitudes cause the contour lines to shift somewhat. In addition, fast solar wind is scattered in the (β_{\parallel}, ξ) space, with values of ξ and β_{\parallel} in the range $0.4 \lesssim \xi \lesssim 3$ and $0.1 \lesssim \beta_{\parallel} \lesssim 3$, respectively (see e.g. Matteini et al. (2013)). The distribution of solar wind data therefore displays tails that would extend in both the stable and unstable regions. These uncertainties however do not affect the trend that high frequency Alfvénic fluctuations ($f \simeq 10^{-3} - 10^{-2}$ Hz) are expected to decay, and that the region of instability in parameter space broadens while approaching the Sun, extending in this way the range of unstable modes towards the lower frequencies. Although it remains to be investigated where Alfvénic periods are located in such diagrams, we argue that signatures of parametric decay – such as increased content of compressive and inwards Alfvén modes, and perhaps a steep radial decrease of amplitudes – should be more evident at heliocentric distances around $r = 0.3$ AU and below, soon to be explored by the upcoming mission Parker Solar Probe (Fox et al. 2016).

5. SUMMARY

We have discussed under which conditions a monochromatic, circularly polarized Alfvén wave constitutes an exact nonlinear state in an anisotropic plasma and we have studied its stability to parametric decay within the CGL framework. We have found that in general the growth rates and the range of unstable modes of the paramet-

ric instability increase with the ratio $p_{0\perp}/p_{0\parallel}$, and that the background anisotropy introduces a new unstable regime: for $p_{0\perp}/p_{0\parallel}$ less than a critical value $\xi^* \simeq 2.67$ the decay is strongly suppressed at increasing values of β_{\parallel} – unless the amplitude of the mother Alfvén wave scales as $\beta_{\parallel}^{1/2}$ – and it is very similar to parametric decay in MHD; for $p_{0\perp}/p_{0\parallel}$ larger than ξ^* , parametric decay occurs for any β_{\parallel} and, in the limit $\beta_{\parallel} \gg 1$, it becomes independent of β_{\parallel} . A comparison with typical values of solar wind plasma beta, anisotropy and amplitudes shows that at $r = 0.9$ AU the solar wind is close to the stable region, while at $r = 0.3$ AU it moves towards the unstable region. Decay signatures should therefore be more evident at heliocentric distances below $r = 0.3$ AU. Since this study relies on the monochromatic assumption, it will be of interest to inspect in future works whether and how the present results change in the case of more general non-monochromatic fluctuations (Cohen & Dewar 1974; Malara and Velli 1996), also by means of numerical simulations in the expanding solar wind generalizing the results of Tenerani & Velli (2013).

Finally, we mention that temperature anisotropy-driven kinetic instabilities may develop for the same values of plasma beta and thermal pressure anisotropy considered for parametric decay, namely, the firehose and the ion-cyclotron instability. These instabilities amplify waves in general at small (kinetic) scales, beyond the validity of the CGL model: it will be necessary to investigate with the help of hybrid-PIC simulations whether and how parametric decay competes and interacts with those kinetic instabilities. However, depending upon plasma parameters, saturation amplitudes of the ion-cyclotron and firehose unstable modes may be smaller than those of Alfvénic fluctuations, and we argue that

in those cases the parametric decay instability should be unaffected.

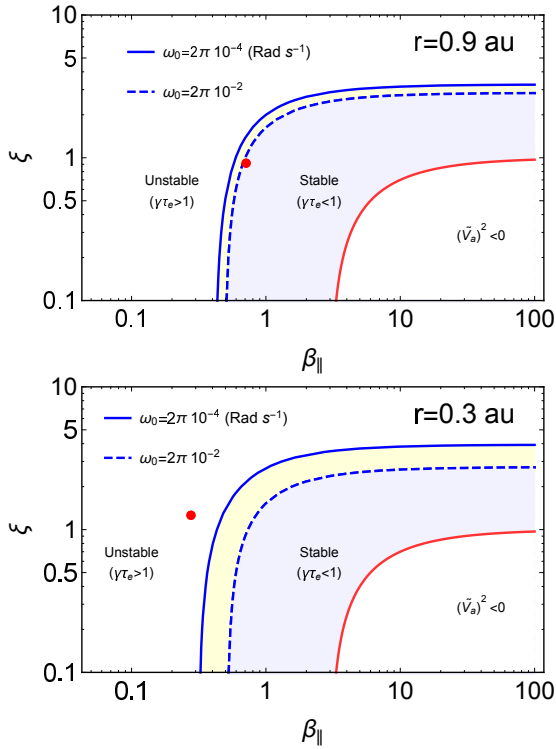


Figure 9. Contours corresponding to $\gamma_m \tau_e = 1$ at two heliocentric distances, $r = 0.9$ AU (upper panel) and $r = 0.3$ AU (lower panel), for high frequency ($\omega_0^h = 2\pi \times 10^{-2}$, dashed line) and low frequency ($\omega_0^l = 2\pi \times 10^{-4}$, solid line) mother waves. At $r = 0.9$ AU the mother wave square amplitude is $(\hat{B}_\perp^h)^2 = 0.01$ and $(\hat{B}_\perp^l)^2 = 0.1$; at $r = 0.3$ AU $(\hat{B}_\perp^h)^2 = 0.05$, and $(\hat{B}_\perp^l)^2 = 0.06$. Only parameters above the red line have been considered for parametric decay: the light blue region is unstable to parametric decay, i.e. $\gamma_m \tau_e > 1$ for $\omega_0 < \omega^h$ while the white region is stable to parametric decay, i.e. $\gamma_m \tau_e < 1$ for $\omega_0 > \omega^l$. The yellow region is the intermediate region where frequencies $\omega^l < \omega_0 < \omega^h$ are unstable. The red dot indicates the location of the average fast solar wind.

This work was supported by grant NNX15AF34G as well as the NASA Solar Probe Plus Observatory Scientist grant. P. H. acknowledges grant 15-10057S of the Czech Foundation.

REFERENCES

Abraham-Shrauner, B., J. Plasma Physics (1967), **1**, 361-378 (1967)
 Chew, G. F., Goldberger M. L., and Low, F. E. Proc. R. Soc. London, Se.A 236, 112–118 (1956).
 Cerri, S. S., Henri, P. Califano, F., Del Sarto, D., Faganello, M., and Pegoraro, F. Phys. of Pl. 20, 112112 (2013).
 Cohen, R. H. & Dewar, R. L., J. Geophys. Res. **79**, 4174–4178 (1974).
 Araneda, J. A. Physica Scripta, **T75**, 164 (1998).

Araneda, J. A., Marsch, E., & Viñas, A. F., Phys. Rev. Letters, **100**, 125003 (2008).
 Bale, S. D., Kasper, J. C., Howes, G. G., *et al.*, Phys. Rev. Letters, **103**, 211101 (2009).
 Bavassano, B., Dobrowolny, F., Mariani, F. and Ness, N. F., J. Geophys. Res. **87** 3617–3622 (1982).
 Bruno, R. & Carbone, V., Living Rev. Sol. Phys. (2013).
 Del Sarto, D., Pegoraro, F. & Califano, Phys. Rev. E 93, (2016).
 Del Sarto, D., Pegoraro, F. & Tenerani, A. Plasma Phys. Control. Fusion 59 (2017).
 Del Zanna, L., Velli, M. & Londrillo, P., Astronomy and Astrophysics, 367, 705 (2001).
 Del Zanna, L., Geophys. Res. Lett., **28**, 2585 (2001).
 Derby, N. F Jr, ApJ 224, 1013–1016 (1978).
 Ferrière, K. M. & André, N., J. Geophys. Res., **107**, 1349 (2002).
 Fox, N. Velli, M., S. D. Bale, R. Decker, A. Driesman, R. A. Howard, J. C. Kasper, J. Kinnison, M. Kusterer, D. Lario, M. K. Lockwood, D. J. McComas, N. E. Raouafi, A. Szabo, Space Science Reviews **204** 7–48 (2016).
 Galeev, A. A., and Oraevskii, V. N., Soviet Phys. Doklady, Engl. transl., 7 988 (1973).
 Gomberoff, L., J. of Geophys. Res., **105** 10509–10518 (2000).
 Hamabata, H. Astrophysical Journal 406, 563–568 (1993).
 Hamabata, H. J. Plasma Physics 49, 29–39 (1993).
 Hellinger, P., Travnicek, P. M., Kasper, J. C., & Lazarus, A. J., Geophys. Res. Lett. 33, L09101 (2006).
 Hellinger, P., Matteini, L., Štverák, S., Travníček, P. M., and Marsch, E., J. Geophys. Res., **16** A09105 (2011).
 Hollweg, J. W., Journal of Geophysical Res. 99, 23431–23447 (1994).
 Hunana, P. Zank, G. P., Goldstein, M., L. Webb, G., M., and Adhikari, L. AIP Conf. Proc. 1720, 030002-1–030002-6 (2016).
 Hunana, P. & Zank, G. P., ApJ 839, 13 (2017).
 Liewer, P. C., Velli, M., & Goldstein, B. E., J. Geophys. Res. 106, 29261 (2001).
 Malara, F., and Velli, M., Phys. Plasmas, **3** 4427 (1996).
 Malara, F., Primavera, L., and Veltri, P., Phys. Plasmas, **7**, 2866 (2000).
 Marsch, E., Space Sci. Rev., **172**, 23 (2012).
 Matteini, L., Landi, S., Hellinger, P., and Velli, M., J. Geophys. Res., **111**, A10101 (2006).
 Matteini, L., Landi, S., Del Zanna, L., Velli, M., and Hellinger, P., Geophys. Res. Lett. 37, L20101 (2010).
 Matteini, L., Hellinger, P., Goldstein, B., Landi, S., Velli, M., & Neugebauer, M., Journal of Geophys. Res. 118, 2771–2782 (2013).
 Matteini, L., Horbury, T. S., Neugebauer, M., and Goldstein, B. E., Geophys. Res. Lett., **41**, 259 (2014).
 Matteini, L., Horbury, T. S., Pantellini, F., Velli, M., and Schwartz, S. J., 802, 1 (2015).
 Nariyuki, Y. & Hada, T., Journal of Geophys. Res. 112, A10107 (2007).
 Passot, T., Sulem, P. L., & Hunana, P., Phys. of Pl. 19, 082113 (2012).
 Jatenco-Pereira, V. Phys. Scr. 113 (1995).
 Sakai, J. I. & Sonnerup, TB. U. Ö. Journal of Geophys. Res., 88 (1983).
 Sulem, P. L. & Passot, T. J. Plasma Physics 81 (2015).
 Squire, J., Quataert, E., & Schekochihin, A. A., ApJL 830 (2016).
 Tenerani, A., Velli, M., J. Geophys. Res. 118, 7507 (2013).
 Umeki, H., and Terasawa, T., J. Geophys. Res. 97, 3113 (1992).
 Unit, T. W. J., & Neugebauer, M., Phys. Fluids 11, 563–568 (1968).
 Vasquez, B. J. J. Geophys. Res. 100, 1779–1792 (1995).
 Wong, H. K. & Goldstein, M. L., Journal of Geophysical Res. 91, 5617–5628 (1986).